Supporting Information for: Direct Measurements of N_2O_5 Reactivity in Salt Lake City Suggest the Aerosol Nitrate Effect Suppresses Additional $PM_{2.5}$ Accumulation

James A. Christie[1,†], Theo Severud[2], Logan Forshee[2], Vanessa Selimovic[2], Siyuan Wang[1], Shatabdi Roy[2], Holly P. Lawson[2], Maria A. Garcia[3], A. Gannet Hallar[3], Haley Humble[3], John C. Lin[3], Paquita Zuidema[1], Kerri A. Pratt[2,4], Cassandra J. Gaston[1,*]

[1]Department of Atmospheric Science, Rosenstiel School for Marine, Atmospheric, & Earth Sciences, University of Miami, Fl 33149, USA

[2]Department of Chemistry, University of Michigan, Ann Arbor, MI 48109, USA

[3]Department of Atmospheric Sciences, University of Utah, Salt Lake City, UT 84112, USA

[4]Department of Earth & Environmental Sciences, University of Michigan, Ann Abor, MI 48109, USA

[†]Present Affiliation: Geophysical Institute, University of Alaska, Fairbanks, AK 99775, USA

[*]Corresponding Author: Email: cgaston@miami.edu, Ph: (305) 421-4979

This Supporting Information (SI) Contains: 21 Pages, 12 Figures, and 5 Tables

Section S1 – Potential Temperature Soundings and Valley Heat Deficit Calculations

Radiosonde soundings at Salt Lake City International Airport (40.790°, -111.977°) were retrieved from the University of Wyoming's atmospheric sounding repository for soundings at 05:00 and 17:00 MST every day throughout the study (archived data can be found at weather.uwyo.edu/upperair/sounding_legacy.html, Site ID 72572). Measurements of radiosonde height in meters and potential temperature in Kelvin (θ) were extracted from the sounding and plotted against the mean ridge mountain height in the Salt Lake Valley to determine periods of relative atmospheric stability, as shown in **Figure S1**.

Another method commonly used to determine periods of relative atmospheric stability in the SLV is the calculation of the valley heat deficit (VHD), which is shown in Equation S1 (Baasandorj et al., 2017; Whiteman et al., 2014):

$$VHD = c_p \int_{1289m}^{2200m} \rho(z)\left[\theta_{2200m} - \theta_{(z)}\right] \quad \text{(ES1)}$$

where 1289 and 2200 m above mean sea level (AMSL) are the valley floor and mean ridgeline elevations in the Salt Lake Valley, θ(z) represents the potential temperature in Kelvin, ρ(z) is the air density in kg/g, c_p is the specific heat of air at constant pressure (kept constant at 1004 J/(kg*K)), and z represents the height in meters. Both θ(z) and ρ(z) were obtained from radiosonde soundings. Days when the VHD is greater than 4.04 MJ/m^2 are indicative of an inversion (Baasandorj et al., 2017; Whiteman et al., 2014). Throughout the field study, there were several days when the VHD exceeded 4.04 MJ/m^2 (see Figure 1a of the main text).

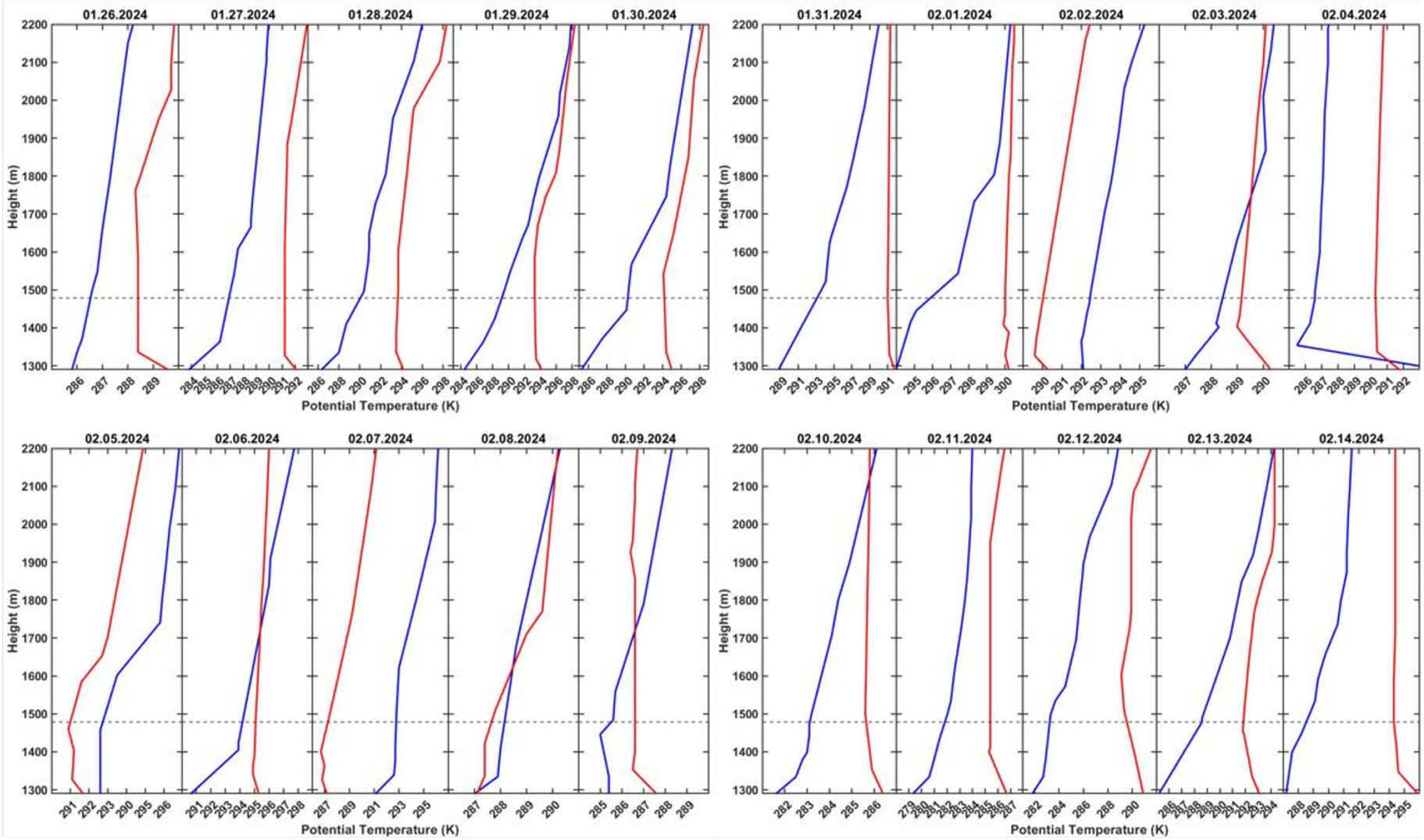

Figure S1: Twice daily potential temperature soundings from January 26, 2024 through February 14, 2024. Blue lines represent the daily 05:00 MST sounding, red lines represent the 17:00 MST sounding, and the grey dotted line represents the approximate height of the sampling inlet during the study.

Section S2 – Additional Information for On-Site Measurements

Section S2.1 – Additional Information on the Ambient Flow Tube and γN_2O_5 Calibrations

The ambient flow tube (AFT) is similar to the AFT described by Bertram et al., 2009, which utilized a 15 cm i.d., 90 cm long, stainless steel tube to measure the reactivity of N_2O_5 with ambient aerosol. A few modifications were made from the initial design from Bertram et al., 2009. First, N_2O_5 was injected into the AFT parallel to the reactor walls, rather than perpendicular to the 1.27 cm i.d. stainless steel tube (the original method described by Bertram et al., 2009). We chose to inject the N_2O_5 parallel to reduce the loss of N_2O_5 to the walls of the flow reactor. Second, the AFT used in this study had stainless steel caps, rather than aluminum caps. The change in material is unlikely to affect N_2O_5 throughput or particle loss to the flow reactor, as all surfaces inside the AFT, including the caps, were coated with Halocarbon wax.

To ensure the validity of γN_2O_5 measured using the AFT, and to also ensure that the reaction remains first order with changes in aerosol reactive surface area concentration ([Sa]), we measured γN_2O_5 at several values of [Sa] using sodium chloride aerosol generated from a commercial standard (NaCl, 99.99% Purity, Thermofischer Inc.) with an atomizer. The tested [Sa] ranged from 86 to 1090 $\mu m^2/cm^3$, with the k_{het} versus [Sa] curve shown in **Figure S2**. The k_{het} calibration produced an average value of γN_2O_5 of 0.032 (± 0.005) and $\varphi ClNO_2$ of 1.1 (± 0.3), where error in this calibration is represented as the 95% confidence interval of the collected uptake coefficients and $ClNO_2$ yields. The precision of collected γN_2O_5 values decreases with [Sa]. For example, the individual standard deviation of γN_2O_5 when [Sa] is 86 $\mu m^2/cm^3$ is ± 0.03, which decreases to 0.004 when [Sa] is 1090 $\mu m^2/cm^3$.

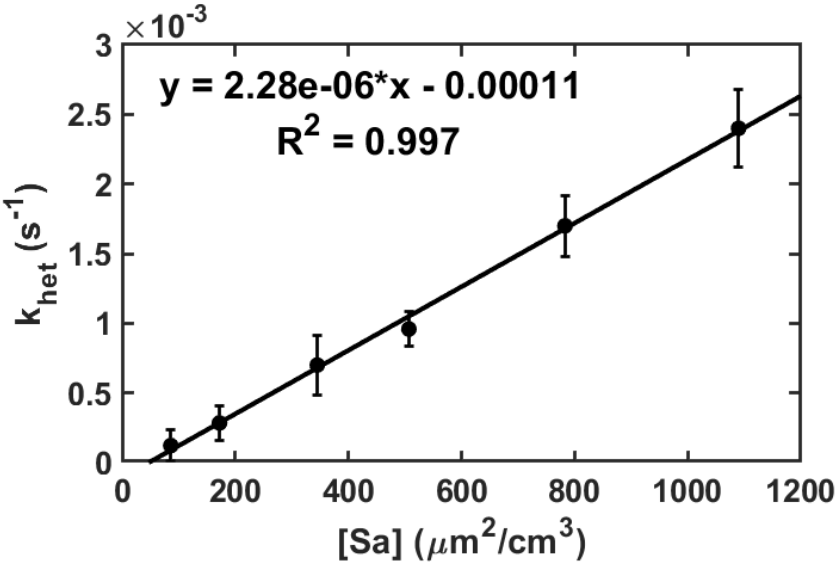

Figure S2: k_{het} versus [Sa] calibration curve using an NaCl standard. Error bars represent the 95% confidence interval.

Several NaCl calibrations were also performed in the field using the chemical ionization mass spectrometer (CIMS) described in Section S2.2. An average value of γN_2O_5 of 0.030 (± 0.004) was measured, which matches the expected value of N_2O_5-NaCl aerosol reactions (Behnke et al., 1997; Gaston and Thornton, 2016; Thornton and Abbatt, 2005), and the [Sa] ranged from 300 to 1500 $\mu m^2/cm^3$ for all field NaCl calibrations.

Section S2.2 – Additional Information on the Chemical Ionization Mass Spectrometer

N_2O_5 and $ClNO_2$ were monitored at a secondary output of the ambient flow tube (AFT) using an iodide (I^-) adduct quadrupole CIMS from THS Instruments (Liao et al., 2011; McNamara et al., 2019). The CIMS measures analytes via the reaction of $I•(H_2O)_n^-$ reagent ions, producing iodide adducts, which are then separated and detected at unit mass resolution using a quadrupole mass analyzer. For CIMS measurements, a critical orifice was placed at the exit of the AFT to reduce N_2O_5-aerosol reactions between the AFT and CIMS, then ~1.3 L/min of airflow was sampled from the critical orifice into a 25 cm long 0.65 i.d. FEP tube and through a 30 °C heated custom three-way valve used for calibration and background measurements (Liao et al., 2011). The $I•(H_2O)_n^-$ reagent ions were produced by passing CH_3I through a ^{210}Po ionizer to produce I^- that were sent into the ion molecule region (IMR), and then water vapor was added from a 1 L water impinger, kept at ~ 25 °C to humidify the reaction chamber to prevent ambient water vapor from affecting the CIMS sensitivity during the study (Liao et al., 2011; McNamara et al., 2019). N_2O_5 in the air from the AFT reacted with the reagent ion in the IMR, held at 15 torr, to produce iodide adduct ions for measurement. Analyte signals were normalized to the reagent ion at m/z 147 ($I•H_2{}^{18}O^-$) to account for minor variations in humidity and detector sensitivity. A list of the 18 measured species, and their respective masses, are available in **Table S1**.

Table S1: CIMS ions, including specific unit mass (*m/z*) and dwell (measurement) time per duty cycle, measured throughout the study.

Ion	m/z	Dwell Time (s)
$I{\bullet}N_2O_5$	235	1.5
$I{\bullet}Cl^{35}NO_2$	208	1
$I{\bullet}Cl^{37}NO_2$	210	0.5
$I{\bullet}H_2O$	147	0.1
$I{\bullet}HNO_3$	190	0.3
NO_3^-	62	0.05
Cl^-	35	0.05
$I{\bullet}Cl_2^{35,35}$	197	0.5
$I{\bullet}Cl_2^{35,37}$	199	0.5
$I{\bullet}Cl_2^{37,37}$	201	0.1
$I{\bullet}Br_2^{79,79}$	285	0.1
$I{\bullet}Br_2^{79,81}$	287	1
$I{\bullet}Br_2^{81,81}$	289	0.1
$I{\bullet}Br^{79}Cl_2^{35}$	241	0.3
$I{\bullet}Br^{79}Cl_2^{37}$	243	1
$I{\bullet}Br^{79}NO_2$	251	0.3
$I{\bullet}Br^{81}NO_2$	253	0.1
$I{\bullet}C_3H_6O_3$	217	0.1
	Cycle Time (s)	7.60

Section S2.3 – Conversion from CIMS Signal (Hz) to Mole Ratio (pptv)

The CIMS was calibrated routinely (twice per hour for 2-minutes) throughout the field study using a commercially available molecular chlorine (Cl_2) permeation source (VICI Metronics) carried by a low flow of ultrapure N_2 (~ 0.2 L/min). Twice per hour, for 3-minutes, an instrument background measurement was conducted by passing airflow through a glass wool scrubber, which removed halogen species, $ClNO_2$, N_2O_5 with >95% efficiency (McNamara et al., 2019). Every day, the output of the permeation source was verified offline by bubbling the Cl_2 gas into a solution of 2% potassium iodide to measure the oxidation production of triiodide (I_3^-) using a UV-visible spectrophotometer at 352 nm (Liao et al., 2011). Since the number of moles of I_3^- should be equivalent to the number of moles of Cl_2, we use Beer's law to calculate the concentration of Cl_2 with a known path length and a molar absorptivity of 23200 $M^{-1}cm^{-1}$.

We then calculate the mole ratios of the analytes of interest (e.g., N_2O_5) using relative sensitivity factors determined by McNamara et al., (2019) and Equation S2:

$$[Analyte]_{ppt,Field} = \frac{Hz_{analyte,Field}}{\frac{\left(\frac{Hz}{ppt}\right)_{analyte,lab}}{\left(\frac{Hz}{ppt}\right)_{Cl_2,lab}} \times \left(\frac{Hz}{ppt}\right)_{Cl_2,Field}} \quad \text{(ES2)}$$

where $[\text{Analyte}]_{\text{ppt,Field}}$ represents the mole ratio of the analytes of interest (such as N_2O_5) in ppt, $Hz_{\text{analyte,Field}}$ is the signal of the analyte in Hz measured in the field, $(Hz/ppt)_{Cl2,Field}$ is the measured Cl_2 signal from the CIMS in Hz relative to the measured concentration of Cl_2, and $(Hz/ppt)_{\text{analyte,lab}}/(Hz/ppt)_{Cl2,lab}$ is the relative sensitivity factor of a specific analyte to Cl_2 (McNamara et al., 2019). The relative sensitivity factors used in this study were reported by McNamara et al., 2019 for the same instrument used in this work and is 0.85 ± 0.08 for N_2O_5:Cl_2.

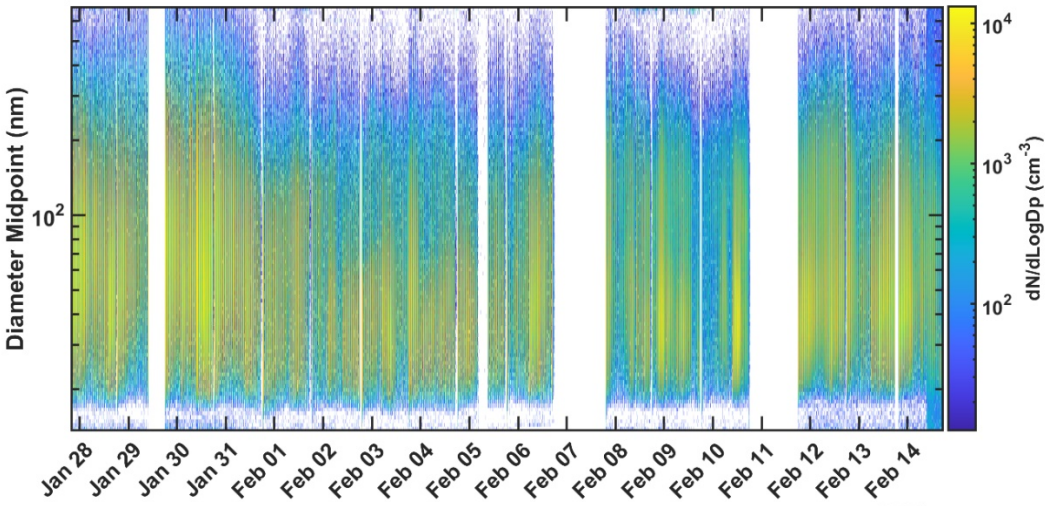

Figure S3: Paper number concentration distribution throughout the study period. The color bar is log-scale.

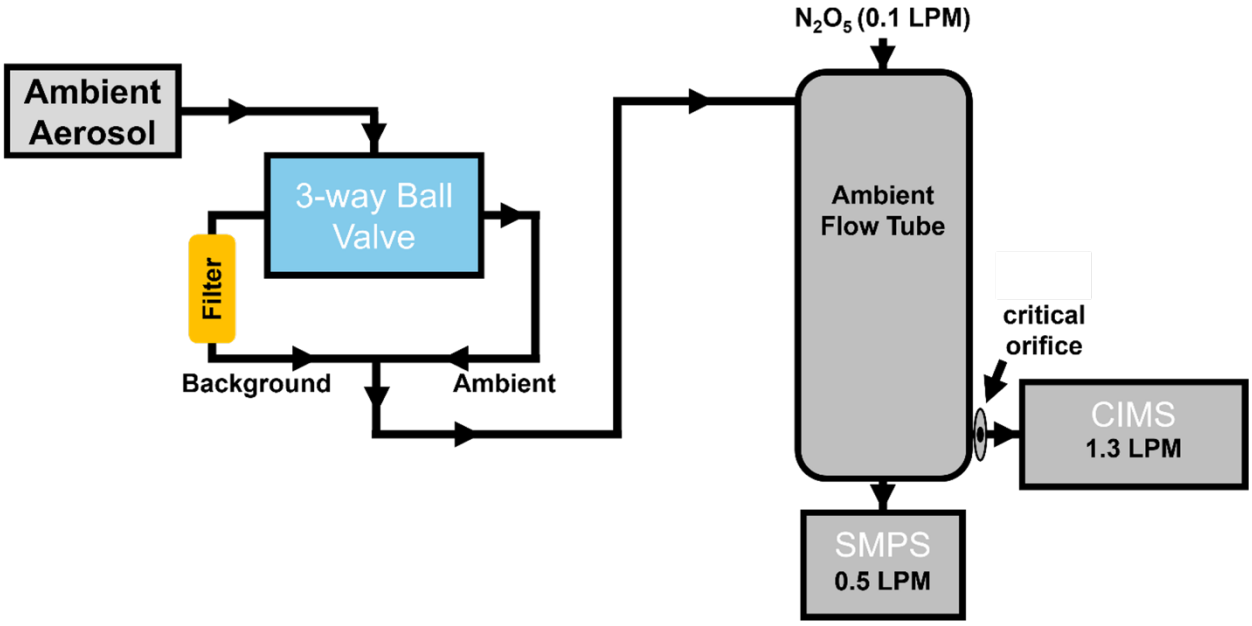

Figure S4: Flow diagram of the ambient flow tube apparatus.

Section S2.4 – Knudsen Number Calculation

Values of γN_2O_5 were calculated using Equation S3 (also Equation 2 of the main text):

$$\frac{1}{\gamma_{N_2O_5}} = \frac{\omega[Sa]}{4k_{het}} - \frac{0.75+0.283\overline{K_n}}{\overline{K_n}+(1+\overline{K_n})} \quad \text{(ES3)}$$

where [Sa] is the aerosol reactive surface area concentration in cm^2/cm^3, ω is the mean molecular speed of N_2O_5 in cm/s (approximately 2.4×10^4 throughout the study but varied with ambient temperature), k_{het} is the first order rate constant calculated in Equation 1 of the main text in s^{-1}, and $\overline{K_n}$ is the dimensionless Knudsen number calculated using Equations S4 and S5:

$$\overline{K_n} = \frac{3D_g}{\omega \overline{r_s}} \quad \text{(ES4)}$$

$$\overline{r_s} = r_p e^{2.5(ln\sigma)^2} \quad \text{(ES5)}$$

where D_g is the gas-phase diffusion coefficient in cm^2/s (~0.1 for N_2O_5, Tang et al., 2014), ω is the mean molecular speed of N_2O_5 used in Equation 2, and r_p and lnσ represent the radius and width of the log-normal particle size distribution respectively measured by the SMPS.

Section S3 – Additional Information on Offline Measurements and Methods

Section S3.1 – MOUDI Filter Extraction and Sample Preparation

Water-soluble inorganic ions were extracted from filters using a similar method to the one described by Gaston et al., 2017. Collected filters were extracted by submerging individual filters in 30 mL of nanopure water (>18 MΩ) in a 50 mL centrifuge tube. The submerged samples were

147 then vortexed for 1 min for 3 repetitions and sonicated for 75 minutes at 60 °C in a water bath to
148 promote ion solvation. Laboratory testing shows that heating the ion solution did not affect
149 concentrations of [NH_4^+] or [NO_3^-]. After cooling for ~ 3 hours at 25 °C, the samples were then
150 vortexed again for 1 minute in triplicate, then the solution was filtered through a 0.22 µm syringe
151 filter (CELLTREAT Scientific Products), with a total water leaching time of ~ 4 hours.

152 Samples were injected into the IC using a 1 mL plastic disposable syringe (Becton,
153 Dickinson and Company) through 0.22 µm syringe filter (CELLTREAT Scientific Products) to
154 remove insoluble particulates from the solution. The cation system utilized a Dionex IonPac™
155 CS12-5 µm (3 x 150 mm) column with a 0.5 mL/min flow rate, 23 mM methanesulfonic acid
156 isocratic separation, and 30 mA suppressor current for an 18-minute run. The anion system used a
157 Dionex IonPac™ AS18 (4 x 250 mm) column and a 1.0 mL/min flow rate of nanopure (> 18 MΩ)
158 water. Anion gradient separation started with 18 mM potassium hydroxide, and linearly increased
159 to 57 mM over 11.5 minutes, then reduced to 18 mM at 11.5 minutes after all the ions had eluted
160 to allow the anion system to equilibrate before the next run, and to create an equal run time to the
161 cation system. The anion system also used a 142 mA suppressor current for the full 18-minute run
162 and the cation system used a CDRS 600 4mm dynamically regenerating suppressor. Instrument
163 calibration used separate cation (Dionex Six Cation-I Standard, Thermo Fisher Scientific,
164 Sunnyvale, CA) and anion (Dionex Anion Standard II, Thermo Fisher Scientific, Sunnyvale, CA)
165 standards to create calibration curves. The method limits of detection were calculated using method
166 blanks, where unused PTFE filters were used in the sample preparation procedure, with the limits
167 of detection for individual ions shown in **Table S2**.

168 **Table S2:** Anion and cation method limits of detection

IC Ions - Limit of Detection (µg/m^3)			
Anions		Cations	
SO_4^{2-}	0.008	Li^+	0.0003
Br^-	0.0001	Na^+	0.02
PO_4^{3-}	0.001	NH_4^+	0.002
Cl^-	0.002	K^+	0.03
NO_2^-	0.00009	Mg^{2+}	0.0006
NO_3^-	0.04	Ca^{2+}	0.01

169

170 ***Section S3.2 – Air Mass Calculation for MOUDI Samples***

171 Chromatograms were manually integrated using the TAG ExploreR iNtegration package
172 (TERN) in Igor Pro and background subtracted from procedural blanks which were prepared
173 using the method discussed in Section S3.1. Liquid concentrations (mg/L) are calculated using
174 calibration curves and converted to air mass concentrations (µg/m^3) using Equation S6:

$$\left(\frac{M \times V_{extraction}}{(Q_{MOUDI} \times t_{sampling}) \times \frac{m^3}{1000\ L}}\right) \times 10^3\ \frac{\mu g}{mg} = \frac{\mu g}{m^3} \quad \text{(ES6)}$$

where M is the liquid concentration of the sample in mg/L, $V_{extraction}$ is the volume used for filter extraction (0.030 L), Q_{MOUDI} is the average flow rate of 30 L/min for the MOUDI during the sampling period, and $t_{sampling}$ is the sampling period in minutes. The air mass concentrations were converted to particle concentrations using Equations S7 and S8:

$$\frac{\left(\frac{\mu g}{m^3}\right)_{air}}{MM_{species}} = M_{air} \quad \text{(ES7)}$$

$$\frac{M_{air}}{[V]} * \frac{mol}{10^6\ \mu mol} * \frac{1000\ cm^3}{L} = M_{particle} \quad \text{(ES8)}$$

where $(\mu g/m^3)_{air}$ is the mass concentration of a species in air, $MM_{species}$ is the molar mass of a species (μg/μmol), [V] is the total particle volume concentration (cm^3/m^3), M_{air} is the molar concentration of a species in air ($\mu mol/m^3$), and $M_{particle}$ is the molar concentration of a species within the aerosol population (mol/L).

Section S4 – Overview of the 1-D Chemical Box Model

Section S4.1 – Prognostic Equations and Turbulent Transport

The model used in this work is built upon, and described by Wang et al., (2020). The temporal evolution of species within the model (dC/dt) is described in Equation S9:

$$\frac{dC}{dt} = \frac{d}{dz}\left(K\frac{\partial C}{\partial z}\right) + P - L - D + PT_{s/p} \quad \text{(ES9)}$$

where C is the concentration of a given species in molec/cm^3 in the gas-phase, the term $\frac{d}{dz}\left(K\frac{\partial C}{\partial z}\right)$ describes vertical transport, *z* represents the midpoint layer height (m), and *K* is the turbulent diffusivity in m^2/s. Values of *P*, *L*, and *D* represent chemical production, loss, and disposition terms, respectively, in molec/cm^3/s. Dry deposition in calculated using resistance-analog methods described by (Wesely, 1989). $PT_{s/p}$ represents the mass transport between the gas- and aqueous-phases in particles previously described by Wang and Pratt, (2017). The differential equations which describe the temporal evolution of chemical species are solved using the Python™ Software (Python™ V.3.12) in ©Google Colab.

The model used in this work consists of 50, 20-meter spaced, vertical layers up to 1000 m. Within the model, atmospheric transport above the surface, and within the boundary layer, is governed by turbulence. The turbulent diffusivity variable *K(z)* is defined by Equations S10 and S11 (Stull, 2012):

$$K = \frac{\kappa z u^* \left(1 - \frac{z}{z_{ABL}}\right)^{1.5}}{\Phi_H(\zeta)} \quad \text{(ES10)}$$

$$u^* = \frac{\kappa U_{ref}}{ln\left(\frac{z_{ref}-d}{z_0}\right)-\Psi_m(\zeta)} \quad \text{(ES11)}$$

where κ is the von Kármán constant ($\kappa = 0.4$), u^* is the friction velocity in m/s, and Z_{ABL} is the atmospheric boundary layer height in meters, estimated from sounding profiles from SLC International Airport (discussed in Section S1). Φ_H is the stability correction for heat, and ζ is a dimensionless term defined as the ratio of Z/L, where L represents the Obukhov length scale in m. U_{ref} is the wind speed in m/s measured at a reference height (z_{ref}, meters), and d is the displacement length in meters, which is typically 70-80% of the height of large roughness elements such as buildings or trees (Stull, 2012). z_0 is the aerodynamic roughness length in meters, ranging from 0.1 to 2 depending on if the simulation is in rural or city center environment (Stull, 2012). For this work, z_0 is set to 0.5. d is the zero plane displacement variable ($0.7 \times z_{ref}$, where z_{ref} is the reference height) and Ψ_m is the integrated form of the stability correction function for momentum.

Under stable conditions, L can be determined by using sounding data as shown in Equation S12 (Arya, 1981):

$$L \cong \frac{u^*\theta}{\kappa g}\frac{\Delta U}{\Delta \theta} \quad \text{(ES12)}$$

where θ is the potential temperature in kelvin, g is the gravitational acceleration constant, and U is the wind speed in m/s. The difference is taken vertically in the atmospheric boundary layer as indicated by the sounding profile. We then use a stability function for stable conditions presented in Equation S13 and S14 (Stull, 2012):

$$\Phi_{m/h} = 1 + 5\zeta \quad \text{(ES13)}$$

$$\Psi_m = -5\zeta \quad \text{(ES14)}$$

The generalized boundary layer conditions are derived from upper air sounding data obtained 05:00 and 17:00 MST on January 3, 2011, at Salt Lake City International Airport. The sounding data at 05:00 is indicative of the boundary layer structure and stability of the night before, while the sounding data at 17:00 is representative of daytime periods. This particular sounding was chosen as several previous studies have previously focused on this PCAP period (e.g., Lareau et al., (2013) and Sun and Holmes, (2019)).

Section S4.2 – Gas-phase and Multiphase Chemistry

Gas-phase chemistry in this model is based on Wang and Pratt, (2017), though bromine chemistry is not included. Additional gas-phase chemical reactions, including C_1-C_4 hydrocarbons (methane, ethane, propane, i-/n-butane) and oxidation products from the Master Chemical Mechanism (MCM), version 3.3.1 (http://mcm.leeds.ac.uk/MCM/) (Jenkin et al., 2003; Saunders et al., 2003) are also included in this model. Heterogeneous reactions are calculated using Equation S15:

$$k_{het} = \frac{1}{4}\gamma_{eff}\bar{v} \times [Sa]_p \quad \text{(ES15)}$$

where k_{het} is the pseudo-first-order rate coefficient in s^{-1}, γ_{eff} is the dimensionless reactive uptake coefficient, and $[Sa]_p$ is the predicted surface area concentration of particles in the simulation in $\mu m^2/cm^3$. $[Sa]_p$ is calculated in the model from the predicted total number concentration of particles and predicted aerosol radius.

Section S4.3 – N_2O_5 Uptake Coefficient

In this work, the N_2O_5 uptake coefficient on particles is calculated using the BT09 parameterization (Bertram and Thornton, 2009), shown in Equation S16:

$$\gamma_{N_2O_5} = A' k'_{2f} \left(1 - \frac{1}{\left(\frac{k_3[H_2O_{(l)}]}{k_{2b}[NO_3^-]}\right) + 1 + \left(\frac{k_4[Cl^-]}{k_{2b}[NO_3^-]}\right)} \right) \quad \text{(ES16)}$$

Here, the rate formation constants for $HNO_{3(aq)}$ and $ClNO_{2(g)}$ are given by k_3/k_{2b} ($6.0 \times 10^{-2} \pm 1.0 \times 10^{-2}$) and k_4/k_{2b} (29 ± 6), respectively (Bertram and Thornton, 2009). Aerosol chloride ($[Cl^-]$; $\mu mol/m^3_{air}$), nitrate ($[NO_3^-]$; $\mu mol/m^3_{air}$), and liquid water ($[H_2O_{(L)}]$; $\mu mol/m^3_{air}$) concentrations were calculated every timestep in the 1-D chemical model. The reaction between aerosol liquid water and $N_2O_{5(aq)}$ is represented by k'_{2f} and is described in Equation S17:

$$k'_{2f} = \beta - \beta e^{(-\delta[H_2O_{(l)}])} \quad \text{(ES17)}$$

where β is $1.15 \times 10^6 \pm 3 \times 10^{-5}$ s^{-1} and δ is $1.3 \times 10^{-1} \pm 5 \times 10^{-2}$ M^{-1} which were determined experimentally by Bertram & Thornton, 2009. The $[H_2O]_{(l)}$ value for Equation S17 is in units of mol/L, rather than $\mu mol/m^3_{air}$.

Under low chloride conditions (Cl^- is < 10% of the total aerosol concentration), we note that the model overpredicts $[H_2O]_{(l)}$ when compared to the E-AIM model (Wexler and Clegg, 2002) (website: https://www.aim.env.uea.ac.ul/aim/aim.php) as shown in **Figure S5** Under conditions where aerosol-chloride is in high concentrations (i.e., when the mole ratio of Cl^- to ($NO_3^- + SO_4^{2-} + NH_4^+$) is greater than 0.1), the model accurately predicts $[H_2O]_{(l)}$. However, when aerosol chloride is in low concentrations (i.e., when the ratio of Cl^- to ($NO_3^- + SO_4^{2-} + NH_4^+$) is less than 0.1), $[H_2O]_{(l)}$ is overpredicted by a factor of ~ 2.66. To correct this, $[H_2O]_{(l)}$ is divided by a factor of 2.66 whenever aerosol-chloride is in low concentration within the model, which shows a strong agreement with E-AIM as shown in **Figure S5**.

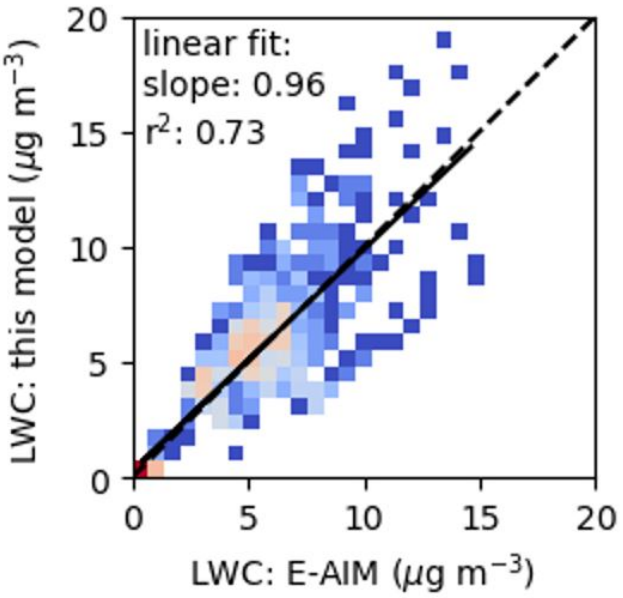

Figure S5: Aerosol liquid water content predicted by the model versus E-AIM using soluble ion inputs from the model showing the relationship between aerosol liquid water between the 1-D model and E-AIM with the correction factor applied.

Table S3: Initial mixing ratios of gas and aerosol species in the 1-D Chemical Model. OC represents organic carbon.

Gas Species (ppbv)		Aerosol Species (μg/m^3)	
O_3	60	Cl	2
CO	100	SO_4	1
NO	0	NO_3	0.01
NO_2	5	NH_4	1
H_2O_2	2	OC	3
CH_4	1900		
C_2H_6	1		
C_3H_8	0.5		
Benene	0.5		
Toluene	0.5		
C_5H_8	0.3		
NH_3	2		

Section S5 – Additional Tables and Figures

Table S4: 24-hr median values of [Sa] and γN_2O_5. Error is reported as the standard deviation of the individual datapoints averaged over the 24-hr period.

Day (yr 2024)	24-hr Median	
	[Sa] ($\mu m^2/cm^3$)	γN_2O_5
01/27 to 01/28	210 ± 60	0.060 ± 0.050
01/28 to 01/29	130 ± 160	0.043 ± 0.028
01/29 to 01/30	410 ± 30	0.020 ± 0.006
01/30 to 01/31	170 ± 100	0.055 ± 0.049
01/31 to 02/01	60 ± 2	0.038 ± 0.050
02/01 to 02/02	60 ± 10	0.115 ± 0.010
02/02 to 02/03	60 ± 20	0.147 ± 0.011
02/03 to 02/04	70 ± 20	0.123 ± 0.025
02/04 to 02/05	54 ± 3	0.086 ± 0.047
02/05 to 02/06	**No Data**	
02/06 to 02/07		
02/07 to 02/08	70 ± 50	0.029 ± 0.0365
02/08 to 02/09	90 ± 50	0.014 ± 0.032
02/09 to 02/10	58 ± 7	0.101 ± 0.020
02/10 to 02/11	**No Data**	
02/11 to 02/12	120 ± 20	0.025 ± 0.016
02/12 to 02/13	70 ± 30	0.036 ± 0.018
02/13 to 02/14	125 ± 30	0.024 ± 0.014

Table S5: Measured soluble inorganic ions measured using ion chromatography. Error is reported as the 95% confidence interval from the triplicate filter measurements.

Day (yr 2024)	Soluble Ion Concentration (μg/m^3)											
	Li^+	Na^+	NH_4^+	K^+	Mg^{2+}	Ca^{2+}	SO_4^{2-}	Br^-	PO_4^{3-}	Cl^-	NO_2^-	NO_3^-
01/27 to 01/28	**BDL**	**BDL**	0.358(±0.004)	**BDL**	0.0015(±0.0007)	0.086(±0.009)	0.12(±0.02)	**BDL**	**BDL**	0.003(±0.003)	0.0080(±0.0004)	0.55(±0.01)
01/28 to 01/29	**BDL**	**BDL**	1.37(±0.04)	**BDL**	0.0051(±0.0007)	**ND**	0.21(±0.02)	0.0005(±0.0004)	0.0014(±0.0002)	**BDL**	0.0048(±0.0004)	4.42(±0.04)
01/29 to 01/30	**BDL**	**BDL**	1.28(±0.01)	**BDL**	0.006(±0.001)	0.039(±0.004)	0.23(±0.02)	**BDL**	**BDL**	0.006(±0.003)	0.0069(±0.0004)	3.30(±0.03)
01/30 to 01/31	**BDL**	0.036(±0.002)	0.433(±0.006)	**BDL**	0.0040(±0.0007)	0.070(±0.006)	0.16(±0.02)	**BDL**	**BDL**	0.003(±0.003)	0.0074(±0.0004)	0.84(±0.01)
01/31 to 02/01	**BDL**	0.024(±0.002)	0.083(±0.002)	**BDL**	0.0026(±0.0007)	0.041(±0.004)	0.07(±0.01)	**BDL**	**BDL**	**BDL**	0.0064(±0.0004)	**BDL**
02/01 to 02/02	**BDL**	0.105(±0.004)	0.073(±0.003)	**BDL**	**BDL**	0.025(±0.004)	0.06(±0.02)	**BDL**	**BDL**	0.03(±0.004)	0.0025(±0.0004)	**BDL**
02/02 to 02/03	**BDL**	0.081(±0.003)	0.098(±0.004)	**BDL**	**BDL**	0.143(±0.009)	0.12(±0.02)	0.0002(±0.0003)	0.0051(±0.0002)	**BDL**	0.0062(±0.0004)	0.194(±0.008)
02/03 to 02/04	**BDL**	0.213(±0.004)	0.098(±0.003)	0.032(± 0.001)	**BDL**	0.116(±0.008)	0.11(±0.02)	**BDL**	0.0045(±0.0003)	0.066(±0.005)	0.0046(±0.0004)	0.32(±0.01)
02/04 to 02/05	**BDL**	0.333(±0.006)	0.069(±0.005)	0.096(± 0.002)	0.0020(±0.0007)	0.231(±0.009)	0.12(±0.02)	**BDL**	**BDL**	0.120(±0.006)	0.0054(±0.0004)	0.81(±0.01)
02/05 to 02/06 02/06 to 02/07	**No Data**											
02/07 to 02/08	**BDL**	0.205(±0.005)	0.159(±0.004)	0.131(± 0.002)	0.0014(±0.0007)	0.087(±0.007)	0.15(±0.02)	**BDL**	**BDL**	0.088(±0.007)	0.0057(±0.0004)	0.86(±0.01)
02/08 to 02/09	0.0024(±0.0002)	0.264(±0.005)	0.171(±0.003)	0.12(± 0.02)	0.003(±0.001)	0.225(±0.008)	0.25(±0.02)	0.0015(±0.0005)	0.0034(±0.0002)	0.200(±0.007)	0.0051(±0.0004)	0.77(±0.01)
02/09 to 02/10	**BDL**	0.062(±0.002)	0.15(±0.02)	0.031(± 0.001)	**BDL**	0.069(±0.006)	0.09(±0.02)	**BDL**	**BDL**	0.013(±0.005)	0.0049(±0.0004)	0.29(±0.01)
02/10 to 02/11	**BDL**	0.192(±0.005)	0.25(±0.01)	0.065(± 0.002)	**BDL**	0.26(±0.01)	0.24(±0.02)	0.0002(±0.0003)	**BDL**	0.066(±0.005)	0.0090(±0.0004)	0.96(±0.01)
02/11 to 02/12	0.0026(±0.0002)	0.244(±0.005)	0.526(±0.008)	0.095(± 0.002)	**BDL**	0.270(±0.009)	0.28(±0.02)	0.0003(±0.0004)	**BDL**	0.003(±0.003)	0.0137(±0.0004)	2.03(±0.02)
02/12 to 02/13	**BDL**	0.748(±0.009)	0.186(±0.006)	0.401(± 0.004)	0.0037(± 0.0007)	0.60(±0.01)	0.26(±0.02)	0.0006(±0.0005)	**BDL**	0.397(±0.009)	0.0110(±0.0004)	2.90(±0.03)
02/13 to 02/14	**BDL**	0.81(±0.01)	0.208(±0.003)	0.380(± 0.004)	0.0021(± 0.0007)	0.49(±0.01)	0.29(±0.02)	0.0009(±0.0005)	**BDL**	0.53(±0.01)	0.0142(±0.0004)	3.00(±0.02)

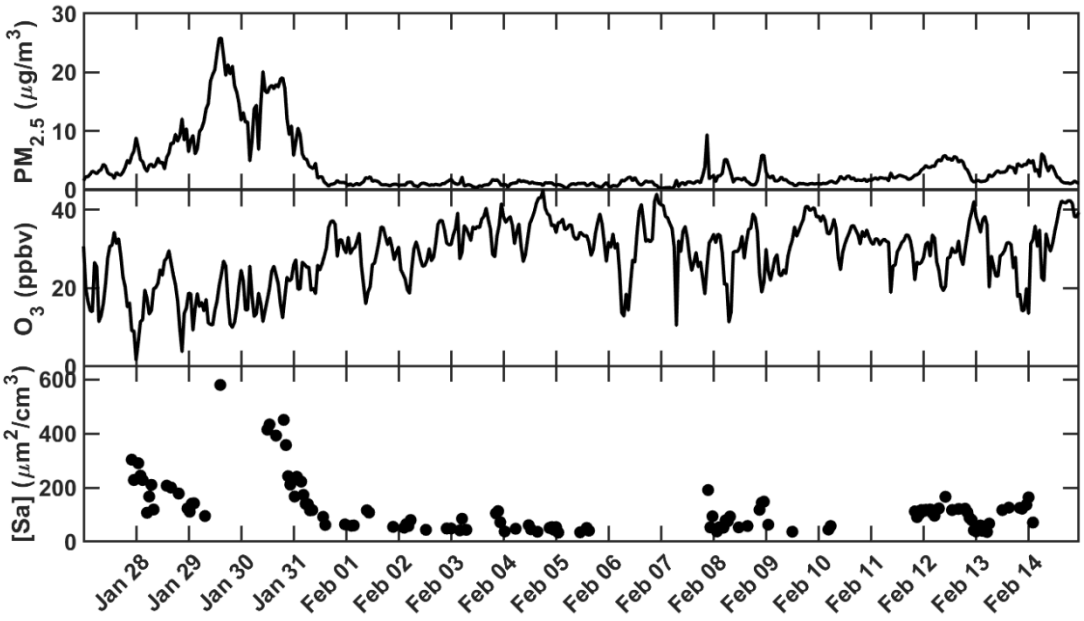

Figure S6: Timeseries of concentrations of ambient $PM_{2.5}$ (top) and O_3 (middle), and aerosol less than 1 μm surface area concentration [Sa] (bottom) at the exit of the AFT when sampling.

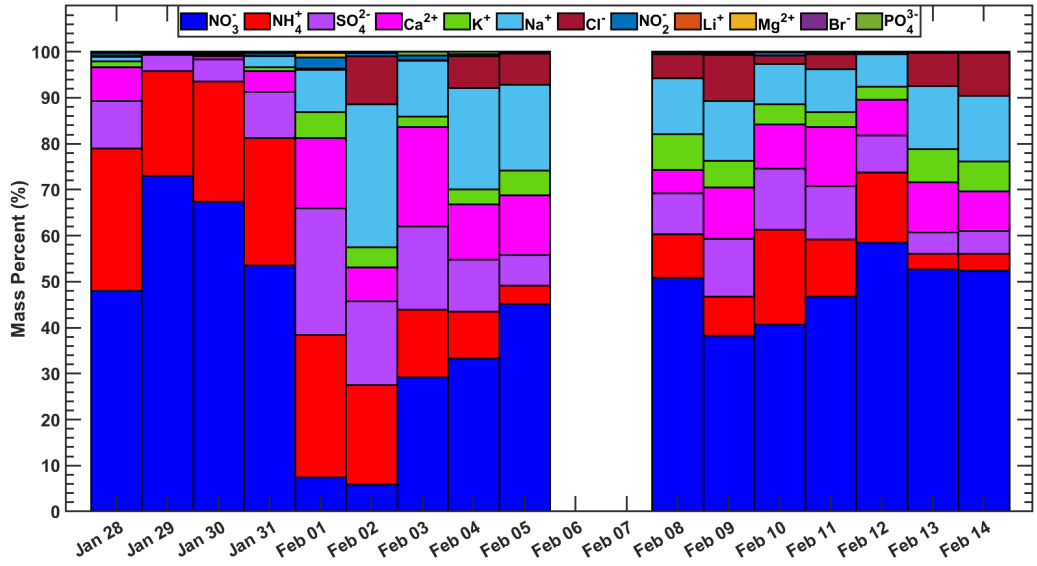

Figure S7: Daily $PM_{0.18\text{-}1.8}$ soluble ion mass fraction, as measured by IC. from January 27 to February 14, 2024.

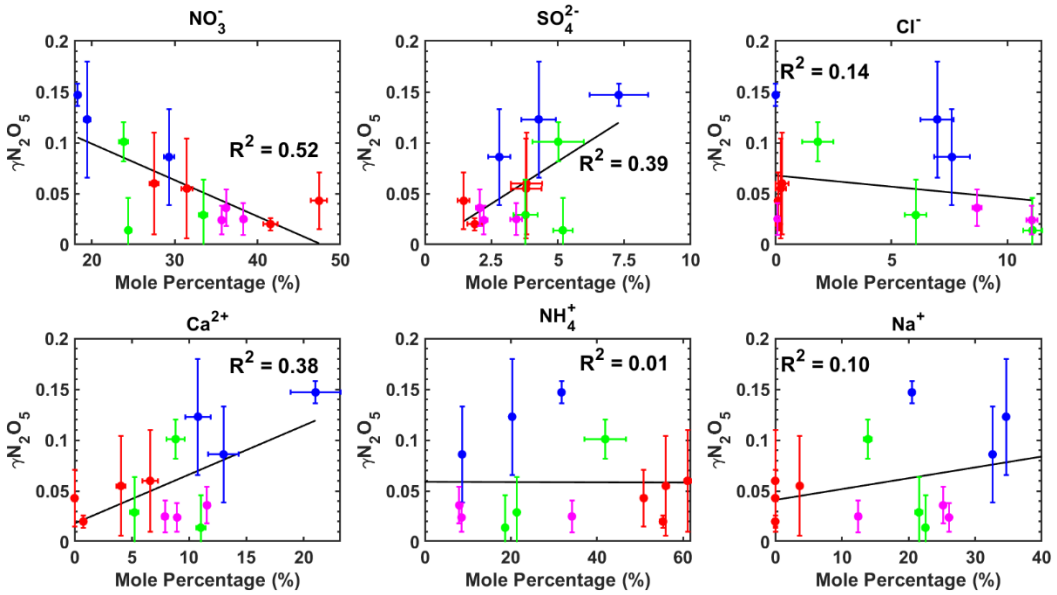

287

288 **Figure S8:** Correlation plots between daily mole percentages of individual ions sampled using
289 IC and 24-hr median values of γN_2O_5. Error bars for the mole percentage values are the 95%
290 confidence interval from triplicate IC measurements, and error bars for the 24-hr median values
291 of γN_2O_5 are the standard deviation of individual γN_2O_5 measurements. Markers follow the same
292 color formatting as the main text.

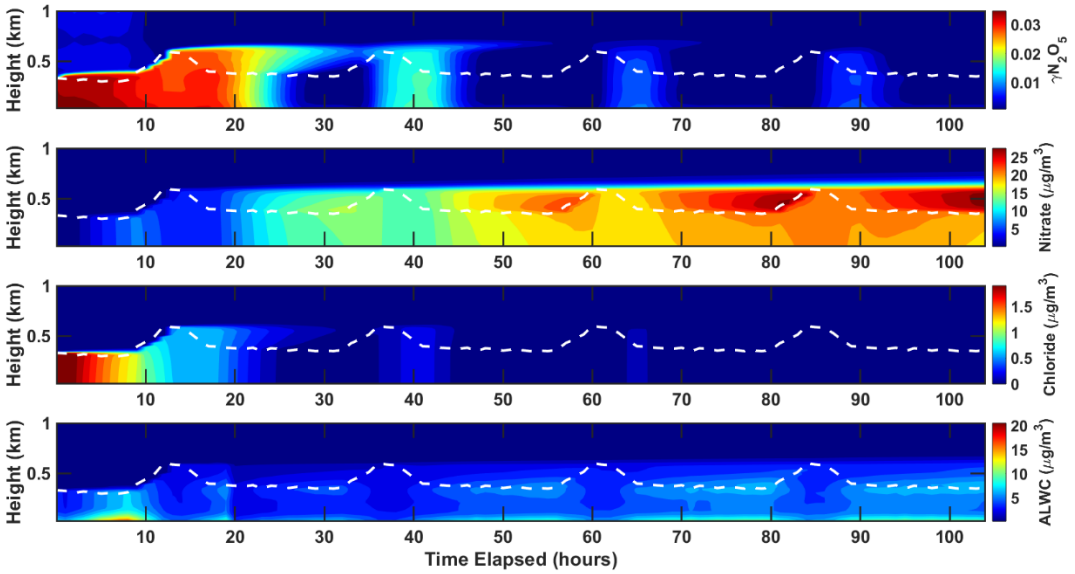

293

294 **Figure S9:** 10 hour spin-up period and 4-day time series of γN_2O_5, NO_3^-, Cl^-, and aerosol liquid
295 water content from the 1-D model run shown in Figure 3 of the main text. The white dashed line
296 represents the planetary boundary layer height (PBLH, above ground level (AGL)), and the
297 difference between the daytime and nighttime PBLH is the nighttime residual layer.

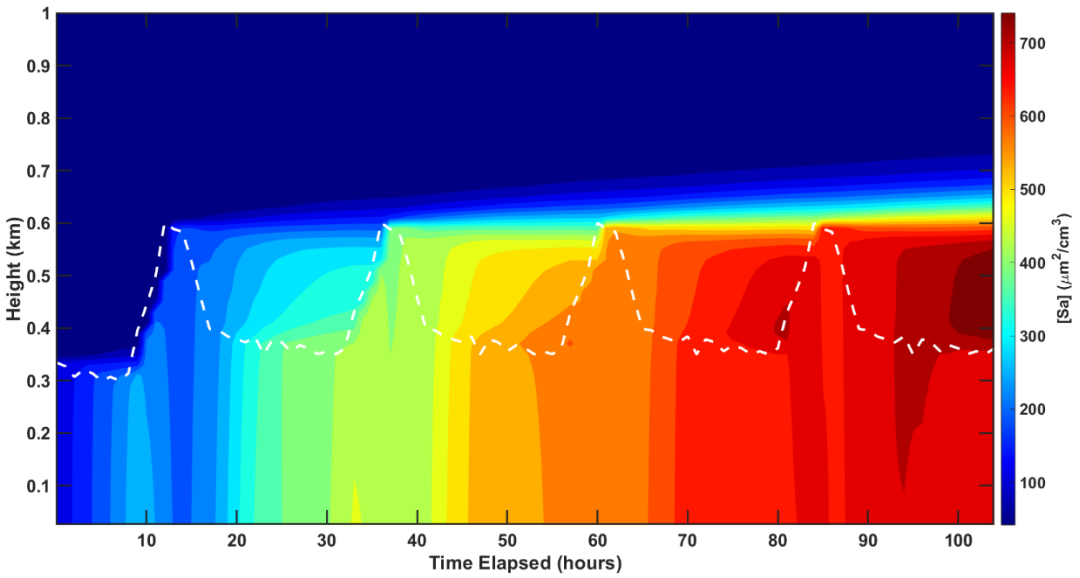

298

299 **Figure S10:** 4-day timeseries, and 10 hour spin-up time, of [Sa] from the 1-D model run
300 discussed in Figure 3. The white dashed line represents the PBLH, and the difference between
301 the daytime and nighttime PBLH is the nighttime residual layer.

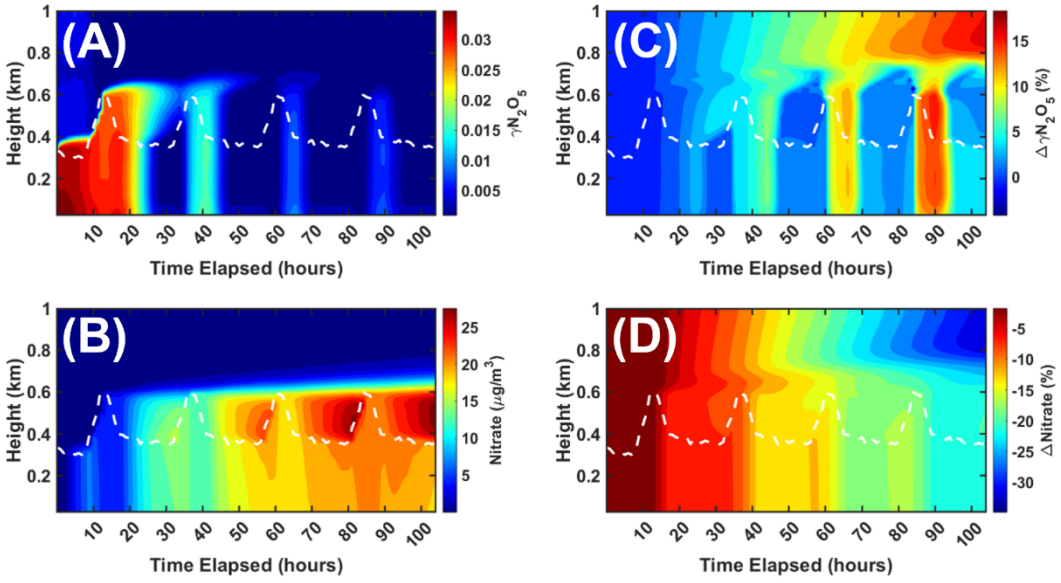

302

303 **Figure S11:** Timeseries (4-day), with 10 hour spin-up time, from the 1-D model where (A)
304 shows values of γN_2O_5 for the background case with identical conditions to the run shown in
305 Figure 3 and (B) shows NO_3^- production under identical conditions to Figure 3. Both (C) and (D)
306 show the change in γN_2O_5 and NO_3^- when the daytime OH-oxidation mechanism to produce
307 NO_3^- is disabled. The white dashed line represents the PBLH.

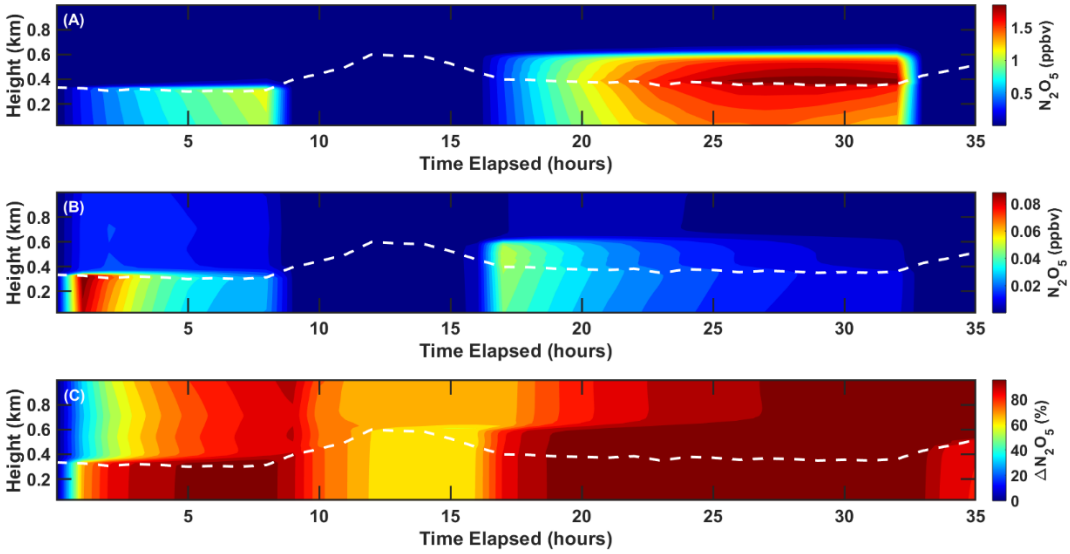

Figure S12: 1-day timeseries used to simulate the sensitivity tests in Figure 4. (A) Simulated concentrations of N_2O_5 when $\gamma N_2O_5 = 0.001$. (B) Simulated concentrations of N_2O_5 when $\gamma N_2O_5 = 0.1$. (C) Percent difference between (A) and (B). The white dashed line represents the PBLH.

Section S6 – References

Arya, S. P. S.: Parameterizing the Height of the Stable Atmospheric Boundary Layer, Journal of Applied Meteorology, 20, 1192–1202, 1981.

Baasandorj, M., Hoch, S. W., Bares, R., Lin, J. C., Brown, S. S., Millet, D. B., Martin, R., Kelly, K., Zarzana, K. J., Whiteman, C. D., Dube, W. P., Tonnesen, G., Jaramillo, I. C., and Sohl, J.: Coupling between Chemical and Meteorological Processes under Persistent Cold-Air Pool Conditions: Evolution of Wintertime PM2.5 Pollution Events and N2O5 Observations in Utah's Salt Lake Valley, Environ. Sci. Technol., 51, 5941–5950, https://doi.org/10.1021/acs.est.6b06603, 2017.

Bertram, T. H. and Thornton, J. A.: Toward a general parameterization of N2O5 reactivity on aqueous particles: the competing effects of particle liquid water, nitrate and chloride, Atmos. Chem. Phys., 9, 8351–8363, 2009.

Bertram, T. H., Thornton, J. A., and Riedel, T. P.: An experimental technique for the direct measurement of N2O5; reactivity on ambient particles, Atmos. Meas. Tech., 2, 231–242, https://doi.org/10.5194/amt-2-231-2009, 2009.

Custard, K. D., Pratt, K. A., Wang, S., and Shepson, P. B.: Constraints on Arctic Atmospheric Chlorine Production through Measurements and Simulations of Cl2 and ClO, Environ. Sci. Technol., 50, 12394–12400, https://doi.org/10.1021/acs.est.6b03909, 2016.

Gaston, C. J., Riedel, T. P., Zhang, Z., Gold, A., Surratt, J. D., and Thornton, J. A.: Reactive uptake of an isoprene-derived epoxydiol to submicron aerosol particles, Environ. Sci. Technol., 48, 11178–11186, https://doi.org/10.1021/es5034266, 2014.

Gaston, C. J., Pratt, K. A., Suski, K. J., May, N. W., Gill, T. E., and Prather, K. A.: Laboratory Studies of the Cloud Droplet Activation Properties and Corresponding Chemistry of Saline Playa Dust, Environ. Sci. Technol., 51, 1348–1356, https://doi.org/10.1021/acs.est.6b04487, 2017.

Jenkin, M. E., Saunders, S. M., Wagner, V., and Pilling, M. J.: Protocol for the development of the Master Chemical Mechanism, MCM v3 (Part B): tropospheric degradation of aromatic volatile organic compounds, Atmos. Chem. Phys., 3, 181–193, https://doi.org/10.5194/acp-3-181-2003, 2003.

Kelly, K. E., Kotchenruther, R., Kuprov, R., and Silcox, G. D.: Receptor model source attributions for Utah's Salt Lake City airshed and the impacts of wintertime secondary ammonium nitrate and ammonium chloride aerosol, J. Air Waste Manage. Assoc., 63, 575–590, https://doi.org/10.1080/10962247.2013.774819, 2013.

Lareau, N. P., Crosman, E., Whiteman, C. D., Horel, J. D., Hoch, S. W., Brown, W. O. J., and Horst, T. W.: The persistent cold-air pool study, Bull. Am. Meteorol. Soc., 94, 51–63, https://doi.org/10.1175/BAMS-D-11-00255.1, 2013.

Liao, J., Sihler, H., Huey, L. G., Neuman, J. A., Tanner, D. J., Friess, U., Platt, U., Flocke, F. M., Orlando, J. J., Shepson, P. B., Beine, H. J., Weinheimer, A. J., Sjostedt, S. J., Nowak, J. B., Knapp, D. J., Staebler, R. M., Zheng, W., Sander, R., Hall, S. R., and Ullmann, K.: A comparison of Arctic BrO measurements by chemical ionization mass spectrometry and long path-differential optical absorption spectroscopy, J. Geophys. Res., 116, D00R02, https://doi.org/10.1029/2010JD014788, 2011.

McDuffie, E. E., Womack, C. C., Fibiger, D. L., Dube, W. P., Franchin, A., Middlebrook, A. M., Goldberger, L., Lee, B. H., Thornton, J. A., Moravek, A., Murphy, J. G., Baasandorj, M., and Brown, S. S.: On the contribution of nocturnal heterogeneous reactive nitrogen chemistry to particulate matter formation during wintertime pollution events in Northern Utah, Atmos. Chem. Phys., 19, 9287–9308, https://doi.org/10.5194/acp-19-9287-2019, 2019.

McNamara, S. M., Raso, A. R. W., Wang, S., Thanekar, S., Boone, E. J., Kolesar, K. R., Peterson, P. K., Simpson, W. R., Fuentes, J. D., Shepson, P. B., and Pratt, K. A.: Springtime Nitrogen Oxide-Influenced Chlorine Chemistry in the Coastal Arctic, Environ. Sci. Technol., 53, 8057–8067, https://doi.org/10.1021/acs.est.9b01797, 2019.

Riedel, T. P., Bertram, T. H., Ryder, O. S., Liu, S., Day, D. A., Russell, L. M., Gaston, C. J., Prather, K. A., and Thornton, J. A.: Direct N2O5 reactivity measurements at a polluted coastal site, Atmos. Chem. Phys., 12, 2959–2968, https://doi.org/10.5194/acp-12-2959-2012, 2012.

Saunders, S. M., Jenkin, M. E., Derwent, R. G., and Pilling, M. J.: Protocol for the development of the Master Chemical Mechanism, MCM v3 (Part A): tropospheric degradation of non-aromatic volatile organic compounds, Atmos. Chem. Phys., 3, 161–180, https://doi.org/10.5194/acp-3-161-2003, 2003.

Stull, R. B.: An Introduction to Boundary Layer Meteorology, Spring Science & Business Media, 2012.

Sun, X. and Holmes, H. A.: Surface turbulent fluxes during persistent cold-air pool events in the salt lake valley, Utah. Part I: Observations, J. Appl. Meteorol. Climatol., 58, 2553–2568, https://doi.org/10.1175/JAMC-D-19-0053.1, 2019.

Tang, M. J., Schuster, G., and Crowley, J. N.: Heterogeneous reaction of N2O5 with illite and Arizona test dust particles, Atmos. Chem. Phys., 14, 245–254, https://doi.org/10.5194/acp-14-245-2014, 2014.

Wang, S. and Pratt, K. A.: Molecular Halogens Above the Arctic Snowpack: Emissions, Diurnal Variations, and Recycling Mechanisms, Journal of Geophysical Research: Atmospheres, 122, https://doi.org/10.1002/2017JD027175, 2017.

Wang, S., McNamara, S. M., Kolesar, K. R., May, N. W., Fuentes, J. D., Cook, R. D., Gunsch, M. J., Mattson, C. N., Hornbrook, R. S., Apel, E. C., and Pratt, K. A.: Urban Snowpack ClNO2 Production and Fate: A One-Dimensional Modeling Study, ACS Earth Space Chem., 4, 1140–1148, https://doi.org/10.1021/acsearthspacechem.0c00116, 2020.

Wesely, M. L.: Parameterization of surface resistances to gaseous dry deposition in regional-scale numerical models, Atmospheric Environment (1967), 23, 1293–1304, https://doi.org/10.1016/0004-6981(89)90153-4, 1989.

Whiteman, C. D., Hoch, S. W., Horel, J. D., and Charland, A.: Relationship between particulate air pollution and meteorological variables in Utah's Salt Lake Valley, Atmos. Environ., 94, 742–753, https://doi.org/10.1016/j.atmosenv.2014.06.012, 2014.